A millimeter magnetic trap for a dual (^{85}Rb and ^{87}Rb) species atom interferometer

J. Alibert, B. Décamps, M. Bordoux, B. Allard, and A. Gauguet

Citation: Review of Scientific Instruments **88**, 113115 (2017);
View online: https://doi.org/10.1063/1.4997149
View Table of Contents: http://aip.scitation.org/toc/rsi/88/11
Published by the American Institute of Physics

REVIEW OF SCIENTIFIC INSTRUMENTS **88**, 113115 (2017)

A millimeter magnetic trap for a dual (^{85}Rb and ^{87}Rb) species atom interferometer

J. Alibert, B. Décamps, M. Bordoux, B. Allard, and A. Gauguet[a)]
Laboratoire Collision Agrégats Réactivité, IRSAMC, Université de Toulouse, CNRS, UPS, Toulouse, France

(Received 21 July 2017; accepted 9 November 2017; published online 30 November 2017)

We present a magnetic trap for cold atoms near a surface of a millimeter-sized atom chip. The trap allows us to capture a large number of atoms with modest electrical currents (40 A) and to generate large magnetic gradients (>300 G cm^{-1}). Here we report a mixture containing 6×10^9 atoms for the two rubidium isotopes ^{87}Rb and ^{85}Rb. This device does not require cleanroom facilities nor micro-machining technologies which makes its construction easier. In addition our design allows the implementation of an optical dipole trap with a laser beam passing through the chip. *Published by AIP Publishing.* https://doi.org/10.1063/1.4997149

I. INTRODUCTION

Atom interferometry was demonstrated as valuable for many applications in precision metrology. It was used to make competitive measurements of fundamental constants such as the fine structure constant[1] or the Newtonian constant of gravitation.[2] It also proved to be a powerful tool for measuring inertial effects like accelerations[3–5] and rotations.[6,7] This sensitivity to inertial forces is used in various projects for investigating many aspects of fundamental physics such as exploration of short-range forces,[8–12] tests of relativity,[13–15] the weak equivalence principle (WEP),[16–19] and dark-energy models.[20] In addition, the possibility to make atom interferometers with a macroscopic separation between the interferometric paths allows atom-electromagnetic interactions measurements, such as static polarisabilities,[21,22] tune-out wavelength,[23,24] and atom neutrality.[25,26] It is also used to explore quantum physics[27–29] and geometrical phase shifts.[30] Most of these applications in fundamental physics may benefit from Bose-Einstein condensed (BEC) sources[31] to further improve their sensitivity and accuracy. Besides, the WEP requires a dual species BEC source. To a lesser extent, many experiments propose a dual species interferometer in order to exploit their differential sensitivities.

In order to be compatible with applications in atom interferometry, the BEC sources need a high atom number and a high cycle rate. Conventional BEC apparatuses produce samples of 10^5–10^7 atoms within 10-60 s using evaporative cooling. The main limitations are due to the number of atoms initially captured and the rate of the evaporative cooling due to the available atomic density. Atom chips proved to be very efficient BEC sources,[32–34] for instance, a ^{87}Rb BEC with 10^5 atoms within 1 s was achieved.[35] However, BEC mixtures need additional optical traps which are challenging to set up close to an atom chip. Only few experimental apparatuses demonstrated ultracold atoms mixture on an atom chip.[36,37]

In this paper, we focus on the pre-cooling and trapping stages of a dual atomic source suitable for atom interferometry. Our design is based on a millimeter-scale magnetic trap which is a trade-off between the capture efficiency of macroscopic traps and the high confinement of atom chips. A particularity of our design is the simplicity of its implementation since it does not require water cooling and it uses only usual standard machining techniques. We demonstrate the capture of a mixture of 6×10^9 atoms of ^{87}Rb and 5×10^8 atoms of ^{85}Rb in 1.8 s, similar to standard macroscopic traps. Another original feature of our design is the possibility to set up optical potentials through a dichroic substrate. This characteristic is necessary for reaching BEC with ^{85}Rb as it needs Feshbach resonances.[38,39] This feature is also essential to transport the atoms away from the chip surface which is required to achieve atom interferometers in a fountain configuration. The dichroic substrate solution is complementary to more advanced integrated optics systems.[40]

The paper is structured in the following manner. In Sec. II we describe the experimental setup. Section III presents the results obtained with the millimeter magnetic trap, and Sec. IV concludes with a summary and an outlook toward the high-flux BEC mixture source.

II. APPARATUS

A. System layout

The goal of the experiment is to make an atom interferometer with a large spatial separation between the interferometric paths. The atom interferometer is based on a fountain type experiment which was designed in the perspective of precision measurements of the atom-electromagnetic interactions.

Atoms are loaded in a Magneto-Optical Trap (MOT) from a beam of rubidium atoms pre-cooled in a two-dimensional Magneto-Optical Trap (2D-MOT). The MOT is created close to the surface trap in a mirror-MOT configuration.[32] As shown in Fig. 1, the surface trap is arranged parallel to the direction of gravity. A set of magnetic coils in a quasi anti-Helmholtz configuration produces a quadrupole field centered at the crossing of the mirror-MOT beams. The atoms are then loaded in a

a)gauguet@irsamc.ups-tlse.fr

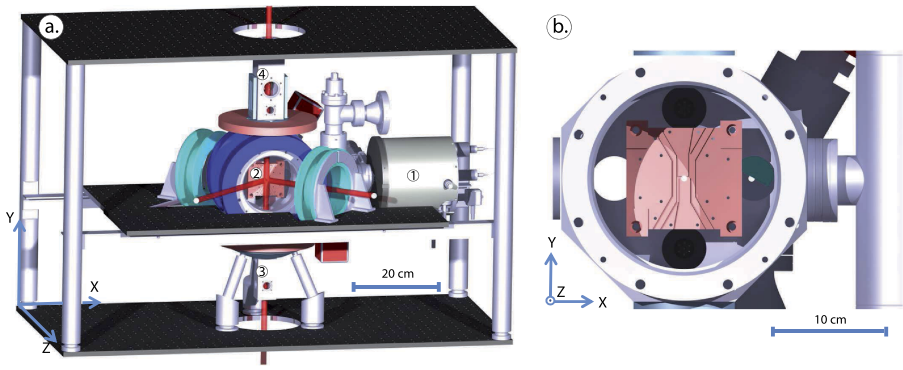

FIG. 1. Atom interferometer apparatus: (a) The figure shows the 2D-MOT ①, the chip chamber ②, the lower ③, upper ④ interferometer chambers, and the mirror-MOT beams (red beams). All the surrounding metallic parts are partially isolated to prevent the formation of eddy currents. The total dimensions of the structure is 120 cm × 79 cm × 60 cm. (b) Zoom in on the magnetic trap set in the chip chamber. The trap is based on a surface Z-wire trap.

magnetic trap based on a surface Z-wire trap, evaporatively cooled using radio-frequency evaporative cooling, and transferred into an Optical Dipole Trap (ODT). BEC will be obtained in the ODT and transported away from the surface with optical beams that pass through the surface. The atom source can be launched vertically with an optical lattice in the upper interferometer chamber or dropped in the lower interferometer chamber. A sequence of pulsed optical lattices allows us to create an atom interferometer. Here, we describe the early stages of this program, which has focused on developing a millimeter trap compatible with atom interferometry applications.

The experimental setup is illustrated in Fig. 1(a). It is based on four vacuum chambers: the 2D-MOT, the chip chamber, and two interferometer chambers. A 5 l s^{-1} ion pump maintains the pressure in the 2D-MOT chamber at about 10^{-8} mbar. The 2D-MOT and the chip chamber are connected through two differential pumping tubes located at each end of an intermediate vacuum chamber. In addition, an ion pump (10 l s^{-1}) and a Non Evaporable Getter (NEG) pump (SAES CapaciTorr-D100®) maintain the pressure in the intermediate chamber at about 1×10^{-9} mbar. The chip chamber is an octagonal titanium chamber. It is 100 mm thick, and the distance between the octagonal faces is 200 mm. The viewports are all indium sealed and anti-reflection coated at 780 nm and 1560 nm. The pressure level in the chip chamber and in the two interferometer chambers is maintained at $\sim 3 \times 10^{-10}$ mbar with an ion pump (10 l s^{-1}) and two NEG pumps (SAES CapaciTorr-D200 and D50). The whole setup was baked out at 110 °C for 15 days.

B. Laser cooling system

The MOT is operated on the D2-line of the two rubidium isotopes ($5S_{1/2} \leftrightarrow 5P_{3/2}$) around 780 nm. The laser cooling system is shown schematically in Fig. 2. The frequency control of the lasers is similar for both isotopes. For each isotope, the repump laser is locked to a saturated absorption line close to the repump transition, and it is used as a master laser. The error signal is generated by using a phase modulation spectroscopy technique with an Electro-Optical Modulator (EOM). The frequency of the cooling laser light is locked to the master laser with an adjustable offset frequency which allows a good frequency tunability. Then, the laser beams pass through Acousto-Optical Modulator (AOM) to adjust the frequency and to quickly control the transmitted light intensity. The four 2D-MOT beams (repump and cooling light for the two isotopes) are amplified with a 1.5 W tapered amplifier. A fraction is used to optically pump the atoms (see Sec. III B). The beams are coupled into polarization-maintaining single mode optical fibers and directed to the vacuum chambers.

The ^{87}Rb lasers are based on two commercially available External Cavity Laser Diodes (ECLDs). The master laser is DL-pro-780 from Toptica® delivering around 60 mW. The laser is locked to the $F = 1 \leftrightarrow F' = 1$–2 saturated crossover line of ^{87}Rb, 78 MHz below the repump frequency ($F = 1 \leftrightarrow F' = 2$). The laser beam is divided into three beams: a fraction (<1 mW) is used for a beat-note with the cooling laser, 30 mW is dedicated to the 2D-MOT, and another 30 mW to the MOT. The repump light for the 2D-MOT and the MOT are frequency shifted (+78 MHz) using independent single pass AOMs. The cooling light is generated with an ECLD (Cheetah Series Laser from Sacher®), amplified with a tapered amplifier (TEC-400-0780-2500 from Sacher) and coupled into a polarization-maintaining single mode fiber. The available power at the fiber output is around 700 mW and distributed to the 2D-MOT and MOT fibers (see Fig. 2). A fraction of the laser power (<1 mW) is picked off to

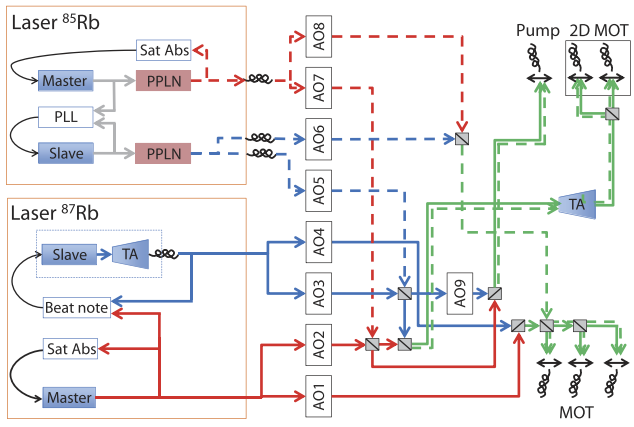

FIG. 2. Laser system for laser cooling. The laser source for ^{87}Rb is based on an ECLD at 780 nm, and the laser source for ^{85}Rb is based on a DFB at 1560 nm which is frequency doubled. The solid lines (respectively dashed lines) represent the laser beams for ^{87}Rb (respectively for ^{85}Rb). Red lines stand for the repump light, blue lines for the cooling light, and green lines represent both cooling and repump light.

interfere with the master laser, the beat-note frequency between the lasers is about 6.5 GHz. After amplification, this signal is converted into a radio-frequency signal by mixing it with a reference signal at 6 GHz from a Voltage Controlled Oscillator (VCO). This signal is then sent to a frequency-to-voltage converter, creating an error signal for the servo-loop. The cooling laser frequency can be adjusted between +5 Γ and −20 Γ around the transition line ($F = 2 \leftrightarrow F' = 3$) within 500 μs by changing the frequency of the VCO, $\Gamma \simeq 6$ MHz being the natural linewidth of the rubidium D2-line.

The laser system used for ^{85}Rb is a compact system commercialized by Muquans®. It is based on fibered optical components at the 1560 nm telecom wavelength. The lasers are two Distributed FeedBack (DFB) laser diodes. The master laser is amplified by an Erbium Doped Fiber Amplifier (EDFA) and frequency doubled with a Periodically Poled Lithium Niobate Wave Guide (PPLN-WG). It is locked to the ($F = 2 \leftrightarrow F' = 1$) saturated line of ^{85}Rb, 93 MHz below the repump frequency ($F = 2 \leftrightarrow F' = 3$). The cooling laser is phase-locked to the repump laser via an optical Phase-Locked Loop (PLL) with an offset frequency of approximately 3 GHz. The cooling laser frequency can be adjusted between +5 Γ and −20 Γ around the transition line ($F = 3 \leftrightarrow F' = 4$) within 100 μs by changing the frequency of the Direct Digital Synthetizer (DDS) which drives the PLL. This commercial laser delivers 280 mW of repump light and 250 mW of cooling light. The repump light for the 2D-MOT and the MOT is frequency shifted using independent single pass AOMs.

This laser system is very robust and capable of operating for long periods (more than a few days) without any adjustment. The linewidth of the lasers is estimated by measuring the beat-notes between the lasers using a frequency analyser, with a 3 ms averaging time. We found a linewidth lower than 600 kHz for all the lasers. Tracking the peak of the beat-notes during long term measurements allows us to measure the frequency drifts of the lasers. These are evaluated with an Allan standard deviation, which remains lower than 200 kHz over 1×10^4 s.

C. Atom surface trap

After the laser cooling stages, the atoms are trapped in a millimeter-scale Ioffe-Pritchard trap based on a Z-trap[32] which has an intermediate size between large cm-scale traps and atom chips (μm-scale). These intermediate sizes, called millimeter-traps, have given rise to various work.[41–45] They have the advantage of large loading volumes compared with the micro-fabricated atom chips and the possibility of substantial field gradients compared with macroscopic traps. Therefore, they are interesting solutions for obtaining BECs with moderate electrical power or as an intermediate step for loading the atoms into a more confining trap such as an atom chip or an ODT. One particularity of our setup lies in the simplicity of its implementation. The Z-wire is made with a 1 mm diameter Kapton® insulated wire [see Fig. 3(a)]. Two parallel wires, I-wires, are added along the Z-wire to increase the longitudinal trapping and an additional loop for the RF knife is used during the forced evaporation cooling. The wires are glued (EPO-TEK 301®) into a 50 mm × 50 mm × 20 mm oxygen free copper support.

The connections with the electrical feedthroughs are ensured by larger (2 mm diameter) copper wires (referred to as the conducting wires). These wires cannot transfer heat to a surrounding bulk. Therefore, three wires in parallel seed the main Z-wire. In this configuration, the conducting wires produce 36 times less heat per unit length than the Z-wire and distribute the heat to multiple feedthroughs. The electrical contact between the chip's wires and the conducting wires is ensured by copper beryllium (CuBe) connectors. At the other end, they are connected to CuBe push-on connectors fixed on 8 feedthrough copper pins. Each pin is specified for a maximum current of 12 A [Fig. 3(b)].

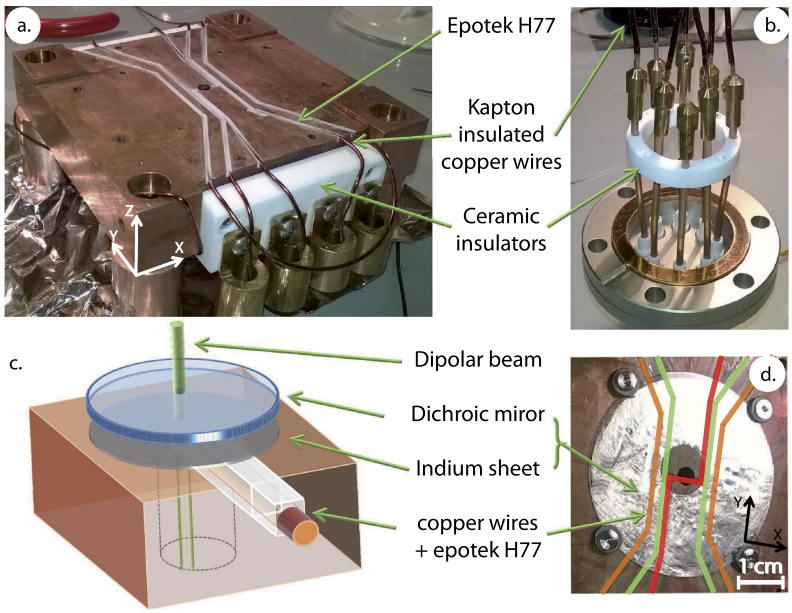

FIG. 3. Millimeter-trap: (a) Picture of the copper mount. (b) Electrical feedthrough. (c) Schematic of the chip including the dichroic mirror. A laser beam (1560 nm) with a waist of 50 μm can pass through a 5 mm diameter hole in the copper mount. (d) Picture of the atom chip with the Z-wire (red), I-wires (green), and the RF-wire (orange). The Z-wire crosses the hole 1 mm below the hole center.

We use the standard Z-trap configuration for the magnetic trap; it consists in a magnetic field minimum produced by the combination of the magnetic field induced by the current $I_z \cdot \mathbf{e}_x$ in the central part of the Z-wire and a homogeneous bias field $B_b \cdot \mathbf{e}_y$ perpendicular to it. The two magnetic fields cancel out at a distance z_0 from the wire creating a quadrupole field which has a zero-field line parallel to the wire. This trap has a transverse trapping frequency ω_t in the y and z directions and almost no longitudinal confinement. In order to provide a three-dimensional confinement, one can bend the end of the wire at 90° which gives its typical Z shape. Those two parallel wires produce a field in the x direction with a minimum $B_0 \cdot \mathbf{e}_x$ that leads to a longitudinal trapping frequency ω_l.

Using an analytic model of infinitely long, thin, and straight wires, one can show that the distance z_0 from the wire is proportional to I_z/B_b, and the magnetic gradients are therefore proportional to $1/z_0^2$. In our case, the thickness of the mirror [see Figs. 3(c) and 4(b)] gives a lower available value for z_0 and thus limits the confinement. The effective trap depth is further lowered by atom-mirror interactions. At a constant height z_0 from the wire, B_0 is proportional to I_z, and the trapping frequencies are $\omega_t \propto \frac{B_b^4}{I_z^2 B_0}$ and $\omega_l \propto I_z$.

Maximizing the confinement is a key parameter for the evaporative cooling through the re-thermalization rate induced by elastic collisions. One can find three ways to increase the trapping frequencies at a constant z_0. The first one is to increase the current I_z in the Z-wire proportionally to the bias field B_b. However, the current in the Z-wire is limited by the Joule effect and heat dissipation. In our case, we set the current to 40 A which corresponds to an increase of 30 °C of the wire temperature in steady state. The second option is to increase the longitudinal confinement using a dedicated pair of straight wires (I-wires) parallel to the side wires of the Z-wire [see Fig. 3(d)]. Finally, we can increase the confinement by reducing B_0, the magnitude of the magnetic field at the bottom of the trap. Since the field at the bottom is aligned with $\mathbf{e}_x$, applying an external homogeneous field (B_{ext}) along $\mathbf{e}_x$ with a pair of dedicated coils pulls down the trap bottom. It results in an increase in the trap depth together with an increase in the confining gradients.

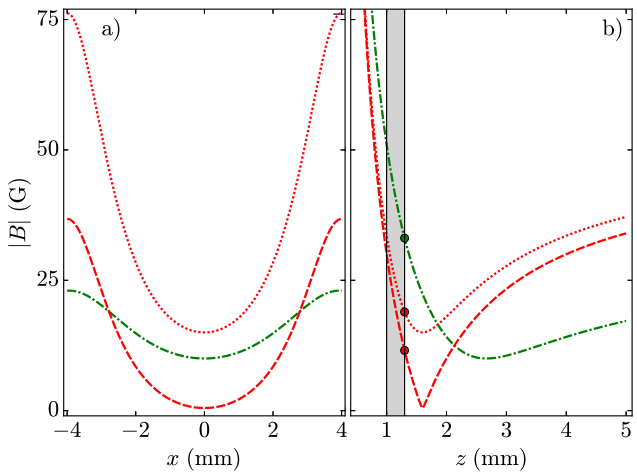

FIG. 4. Simulated cross sections of the magnetic trap along the z (a) and x (b) directions. The bias B_b is aligned with gravity (y direction). Green dotted-dashed lines are related to the capture trap with $B_b = 28$ G. The dashed red lines are typical profiles of a compressed trap using $B_b = 50$ G, I-wires (30 A), and $B_{\text{ext}} = 14.5$ G along x. The orange dotted lines are profiles without B_{ext}. The grey region indicates the dichroic mirror location that limits the trap depths. The maximally trapped states have a temperature conversion factor of 70 μK G^{-1}.

Figure 4 presents three different simulated cross sections of the magnetic field configuration along the z and x directions. The wider trap (dotted-dashed line) is obtained with $I_z = 40$ A and $B_b = 28$ G. This trap, with a large volume and sufficient depth, is used to capture a maximum atom number from the optical molasses. Its frequencies are $\omega_l = 2\pi \times 17$ Hz and $\omega_t = 2\pi \times 64$ Hz. To prepare for the evaporative cooling, this capture trap is compressed by ramping up linearly and simultaneously the bias field to $B_b = 50$ G, the current in the I-wires to 30 A, and also B_{ext} to 14.5 G. The dashed lines in Fig. 4 are typical profiles of such a compressed trap. For comparison, the dotted lines represent the compressed trap with $B_{\text{ext}} = 0$. It emphasizes how B_{ext} modifies the trap depth and transverse trapping frequencies. The final depth is limited to 470 μK due to atom-surface collisions. The trapping frequencies of the most compressed trap available for our experiment are $\omega_l = 2\pi \times 100$ Hz and $\omega_t = 2\pi \times 500$ Hz. For comparison, in Sec. IV, the trap we use is produced with a lower value of B_{ext} for which we expect $\omega_l = 2\pi \times 30$ Hz and $\omega_t = 2\pi \times 114$ Hz.

The second interesting feature of our device is the use of a dichroic mirror to produce the mirror MOT (reflecting light at 780 nm) and an ODT (transmitting light at 1560 nm). This feature improves the optical access which is a disadvantage of the usual surface traps and allows us to focus the optical trap above the Z-wire to optimize its overlap with the magnetic trap. The tested optical characteristics are compatible with the implementation of an ODT, but no tests with cold atoms have been performed yet. The MOT mirror is a 70 mm diameter, 300 μm thick glass substrate. It is transparent at 1560 nm, and one face has a dichroic coating designed to transmit 1560 nm and optimized to have a high reflection coefficient for both incident linear polarizations at 780 nm and for an incidence angle of 45°. However, the design of this optical coating requires a trade-off between the reflectance and the control of the phase shift between the S and P polarizations. We choose to optimize the polarization instead of the reflectance. We measured a reflectivity better than 98% and a transmission higher than 97% (limited by the uncoated substrate face). We checked that a right-handed polarization (Stokes parameter, $S_3 = 0.999$) was transformed into a left-handed polarization (Stokes parameter, $S_3 = -0.990$) after reflection at 45°. A 100 μm thick indium sheet is placed on top of the copper surface to prevent mechanical stress on the rigid mirror. With hindsight, this additional layer reduces the trapping performances, and it might be better to avoid it. In addition to the adhesion on the indium sheet, four titanium screws with handmade indium washers maintain the mirror at the center of the support [see Figs. 3(c) and 3(d)].

D. Imaging system

The atoms are detected by fluorescence imaging techniques. A short light pulse produced by the MOT beams

resonantly excites the atoms with controlled peak intensity. A second pulse, applied after the atoms left the field of view, provides the reference background intensity. Subtracting this offset gives an image of the atom cloud. The fluorescence light is collected using a triplet (CVI®: LAP-250-50-PM + APM-250-50-PM) with an infinite conjugate ratio, and a second doublet (Thorlabs®: AC508-250-B) images the cloud on a CCD camera (GS3-U3-14S5M-C from Pointgrey®). The optical magnification is 2, and the optical resolution is better than 8 μm.

The detection beams are pulsed during 100 μs with zero detuning and a peak intensity of $10 \times I_{sat}$ for ^{85}Rb and of $31 \times I_{sat}$ for ^{87}Rb, where I_{sat} is the saturation intensity of the cooling transitions (~1.67 mW cm^{-2}). Both the detuning and the saturation intensity of the imaging pulse were calibrated independently to ensure an accurate measurement of the atom number. We operate at large intensity and assume that the excitation rate is saturated for all the atoms during the pulse.

Using all three MOT beams to image the MOT cloud allowed us to reach a combined intensity of $\sim 60 \times I_{sat}$ for ^{85}Rb (respectively $186 \times I_{sat}$ for ^{87}Rb). This intensity is sufficient for the MOT characterization, which has an optical thickness below 20. The accuracy of our method is mainly limited by the knowledge of the effective resonant cross section σ_0 in dense clouds, which determines whether the center of the cloud is saturated and how often scattered light is rescattered before reaching the detector. As discussed in Ref. 46, saturated fluorescence imaging has been shown to be accurate for atom number evaluation as long as the saturation parameter is approximately three times larger than the cloud optical thickness. We evaluated that our calibration uncertainty remains below 20%, assuming that the measured σ_0 is constant throughout the cloud and that the 6 orthogonal beams are equally depleted by each atom which radiates isotropically. This evaluation also includes experimental imperfections such as the collection solid angle.

III. EXPERIMENTAL RESULTS

A. Laser cooling and trapping

The complete experimental sequence is summarized in Fig. 5. It starts with the Magneto-Optical Trap (MOT) loaded in 1.8 s from the 2D-MOT. The quadrupole field is characterized by a gradient of 7 G cm^{-1} along the coils axis and 3.5 G cm^{-1} in the orthogonal plan. Three optical fibers provide the cooling and repump light to the three beams of our mirror-MOT configuration. All beams have a beam waist radius of 0.7 mm, and they are circularly polarized with a set of wave plates according to the quadrupole field orientation. The loading is optimized for a red detuning of the cooling light of 2.5 Γ for both ^{85}Rb ($F = 3 \leftrightarrow F' = 4$) and ^{87}Rb ($F = 2 \leftrightarrow F' = 3$). The peak intensity in the center of the MOT is similar to the intensity used for detection.

Figure 6 presents the loading of the mirror-MOT in the cases of the two isotopes loaded separately and of the mixture. The larger natural abundance (72.2%) of ^{85}Rb in our source explains the higher loading rate ($12.4 \pm 0.4 \times 10^{10}$ s^{-1}) for this isotope when loaded alone compared with the one of ^{87}Rb alone ($5.2 \pm 0.4 \times 10^{10}$ s^{-1}). When loaded together, the loading rate of the two isotopes is reduced for both isotopes due to the finite available power in the tapered amplifier providing light for the 2D-MOT. The relative input power and the nonlinear gain of the amplifier gives significantly more ^{87}Rb light. It explains the slight reduction of the loading rate of ^{87}Rb to $3.1 \pm 0.2 \times 10^{10}$ s^{-1}, while the one of ^{85}Rb drops to $1.3 \pm 0.2 \times 10^{10}$ s^{-1}.

After the initial MOT stage, the magnetic gradients are ramped up to 9.5 G cm^{-1} (axial) and 4.8 G cm^{-1} (transverse) and the cooling laser detuning is simultaneously increased to -11 Γ. This realizes a compressed MOT (CMOT) in which the atomic density is increased and the cloud temperature is reduced (see Table I). In addition, B_{ext} is progressively ramped down during the CMOT to transport the magnetic field minimum closer to the surface and thus optimize

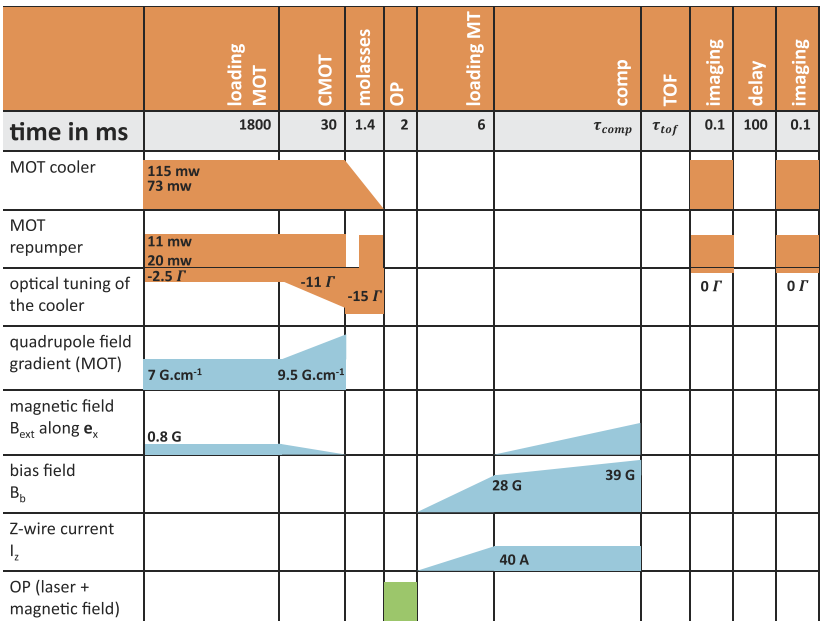

FIG. 5. Experimental sequence. The horizontal axis is not at scale, each step duration is indicated above the graph. OP stands for optical pumping, MT stands for magnetic trap, comp for magnetic trap compression, and TOF for time of flight. Laser powers refer to ^{85}Rb (lower rows) and ^{87}Rb (upper rows).

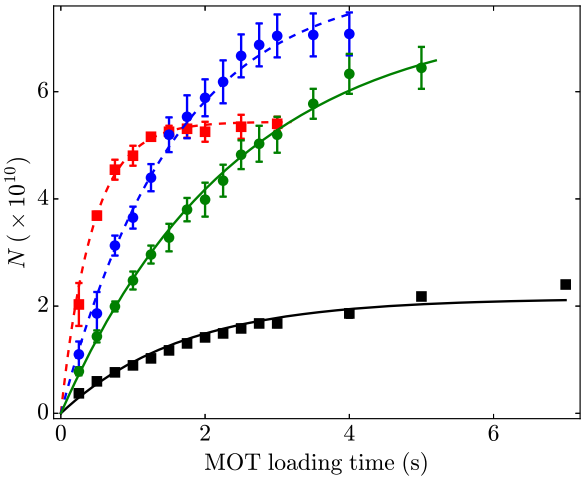

FIG. 6. MOT loading. The collected atom number in the mirror-magneto-optical trap as a function of the loading time for the two isotopes of rubidium, in the case of single species experiments (dashed line) and for the mixture (solid line). The square and circle markers stand for, respectively, ^{85}Rb and ^{87}Rb. Each isotope is imaged individually with resonant light after a 2.2 ms time of flight. The lines are exponential fits from which the loading rate is extracted.

the mode matching between the cloud and the magnetic trap.

To further cool the atomic ensemble below the Doppler limit, all magnetic fields are then turned off, and an optical molasses stage is performed. The laser detuning is increased to $-15\ \Gamma$ for both species for 1.4 ms. The laser intensities are finally ramped down while keeping a non-zero intensity of repump light to ensure that all atoms are in the upper hyperfine level of their respective ground state (F = 3 for ^{85}Rb and F = 2 for ^{87}Rb). All the light beams are switched off, and the cloud is then transferred into the magnetic trap.

B. Magnetic trap loading

The optimal transfer of the laser-cooled atomic ensemble to the conservative millimeter-trap needs a good mode matching between the magnetic trap and the cloud. This is ensured by the high density acquired during the CMOT stage and the low temperature reached with the optical molasses step to fit within the trap depth (1 mK). The relative position of the cloud with respect to the magnetic trap center is set by the position of the CMOT which can be adjusted with homogeneous magnetic fields along x and y directions.

Moreover, after the optical molasses stage, atoms are distributed over all the Zeeman sub-levels of $F = 3$ for ^{85}Rb (respectively $F = 2$ for ^{87}Rb). Therefore, we prepare the atoms into the magnetically trappable states $|\mathrm{F} = 3, m_\mathrm{F} = +3\rangle$ for ^{85}Rb (respectively $|\mathrm{F} = 2, m_\mathrm{F} = +2\rangle$ for ^{87}Rb) using an optical pumping stage. We use a 2 ms light pulse of 60 μW (respectively 160 μW) resonant with the transition $F = 3 \leftrightarrow F' = 3$ (respectively $F = 2 \leftrightarrow F' = 2$). The optical pumping beam is retro-reflected on the chip and carefully aligned with the quantization axis which is defined by a magnetic field oriented along the z axis with a magnitude of 15 G. The optical polarization of the beam is right-handed which induces σ^+ transition, and the beam waist is 3.8 mm. A small amount of repump light for both isotopes is added to the pulse in the same beam. The characteristic parameters of the loaded mixture after 100 ms of hold time in the magnetic trap are presented in the last column of Table I.

To characterize the transfer efficiency, we focus on ^{87}Rb and compare experimental results with numerical predictions. Figure 7 shows the measured atom number in the trap, after 1 s of hold time to ensure thermal equilibrium, as a function of the bias field value B_b for the experiment and our model. For a given current in the Z-wire, the bias field sets simultaneously the trap depth, its distance to the chip and the confinement. At the optimum, ~20% of the atoms measured in the optical molasses are successfully loaded into the magnetic trap. Solid lines in Fig. 7 are predictions from our model which includes the measured parameters of the optical molasses and the currents used to generate the magnetic trap. The model is built as follows.

The magnetic potential is obtained by numerical simulations taking into account the finite size of the wires and the actual external coil shape. This calculation allows us to find the edge of the trap limited by the gravitational potential and

TABLE I. Typical values of the atom number and temperature at the first four stages of the experimental sequence for the dual-isotopes mixture. In each case, the upper row refers to ^{87}Rb, and the lower one refers to ^{85}Rb. Errors indicated in the table are standard errors over 10 realizations of the experiment. The systematic errors (20%) due to the detection are not indicated. For the magnetic trap, we wait 100 ms before performing measurements to let the untrapped atoms fall away. The measurements related to the ^{85}Rb isotope summarized in this table were performed after re-optimization. It explains why the values are not compatible with data shown in Fig. 6.

	MOT (1.8 s)	CMOT	Molasses	Magnetic trap
N ($\times 10^9$)	38 ± 1.2	29 ± 0.3	32 ± 0.2	5.8 ± 0.01
	2.3 ± 0.1	0.5 ± 0.04	1.2 ± 0.04	0.5 ± 0.06
T (μK)	150	110	42	220
	140	70	35	170

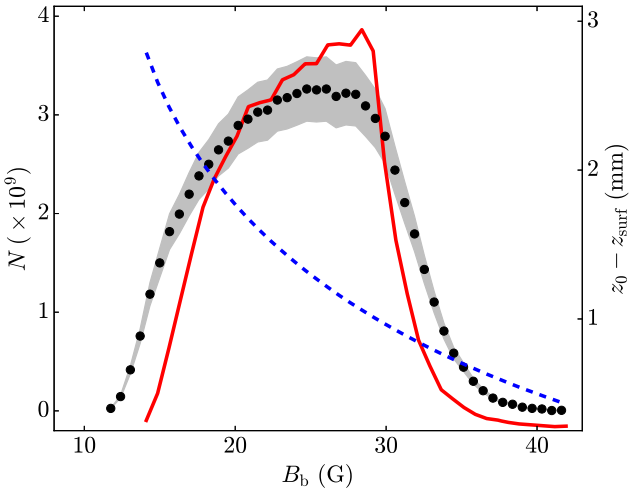

FIG. 7. Captured atom number after a 1 s hold time in the first magnetic trap for a single isotope ^{87}Rb experiment. Dots are the measured atom number. The grey region indicates our uncertainty on the determination of the atom number. The solid line is the prediction of the model described in the main text. The blue dashed line gives the distance between the trap center and the mirror surface $z_0 - z_{\mathrm{surf}}$.

the interaction with the surface. The model also calculates a shift of the trap bottom due to the gravity of (0.2, −0.1, 0) mm along the (x, y, z) directions. We assume that the trap is switched on instantaneously. Therefore, the potential energy of the trap $U(\mathbf{r})$ is added to the energy of each atom at the corresponding position $\mathbf{r}$. In order to evaluate the atom number loaded into the trap, the overlap integral between $U(\mathbf{r})$ and the phase space density distribution of the cloud just after the optical molasses stage is truncated with a cutoff energy corresponding to the trap depth U_0. The same calculation is done to evaluate the internal energy of the atoms remaining into the trap. This calculation takes into account the evaporation process observed during the first few hundreds of milliseconds after the capture. The temperature is evaluated from the atom number and the mean energy, assuming a Maxwell-Boltzmann distribution. Collisions with the residual background gas limit the lifetime in the trap to $\tau = 2.4$ s. We include these additional losses in the model with a scaling factor $e^{-t/\tau}$ to the final atom number. The model is in reasonable agreement with the experimental data (see Fig. 7). In particular, the model reproduces the optimal loading configuration for a bias field of $B_b \simeq 28$ G. Away from this optimal condition, the trap does not overlap with the optical molasses, or its depth is too low.

C. Compressed trap and surface evaporative cooling

The atomic density in the capture trap is too low to perform fast evaporation to BEC. The next step is thus to increase the confinement of the trap as described in Sec. II B. In practice, we limit the current in the Z-wire to $I_z = 40$ A and ramp up the bias field to $B_b = 39$ G and the current in the I-wires to 20 A and the homogeneous external magnetic field to $B_{\text{ext}} = 2.2$ G. This compressed trap is experimentally characterized by a modulation spectroscopy technique.[44] It consists in a small modulation (modulation depth ∼1%) of the current in the Z-wire which modulates the position of the trap center and the confinement in every directions of the trap. When the modulation frequency reaches each trapping frequency and its first harmonics, atom losses are expected due to dipole oscillations damping and parametric heating. The recorded spectrum is shown in Fig. 8.

It presents two peaks around 110 Hz and 220 Hz paired as a fundamental frequency and its second harmonic. It is attributed to the excitation of the transverse confinements ω_t (along y and z directions). We do not detect any resonance attributed to the axial confinement expected around 30 Hz. The energy transferred by a modulation in this frequency range is too low to induce significant losses. We find a good quantitative agreement with the simulated transverse trapping frequencies for those currents and field parameters (expected at 115 Hz). It confirms the accuracy of our simulating tools and calibrations.

The compression described earlier is done in 2 s. As already discussed, it is done together with the decrease of the distance between the trapped atoms and the mirror surface. It causes an energy-selective atom loss which results in an evaporative cooling of the atomic cloud.[47–50] Figure 9 shows temperature measurements for both isotopes in the mixture as the trap is displaced toward the surface over the 2 s long compression.

As the distance to the surface decreases, atoms are lost with the same rate for both isotopes. While the temperature stays approximately constant at the beginning of the compression, it suddenly drops when the distance goes below ∼700 μm. It is interesting to notice that the surface evaporative cooling we observe has the same magnitude for both isotopes even if the number of ^{85}Rb atoms is almost one order of magnitude below the number of ^{87}Rb atoms.

Even if some cooling is observed, the atomic density of our sample is not high enough to lead to an efficient evaporative cooling. Surface losses limit the achievable confinement with the existing trap. This limit can be overcome with a dipole trap making use of the optical access in the middle of our chip or with an extra chip with small wires on the surface.

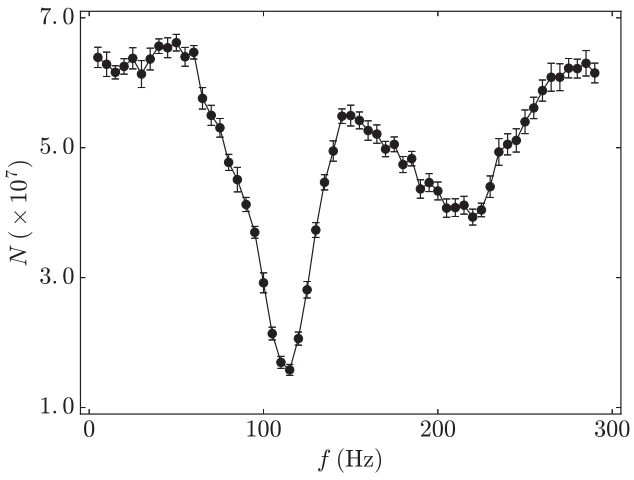

FIG. 8. Modulation spectroscopy of the compressed trap. The figure shows the atom number after 1 s of the I_z current modulation (1%) according to the modulation frequency. Points are the averaged atom number over 14 realizations of the experiment, and error bars correspond to the statistical error of the mean.

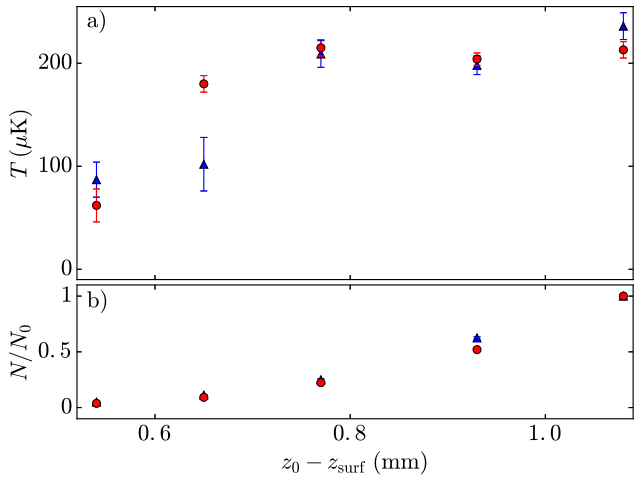

FIG. 9. Surface evaporative cooling: (a) Temperature of ^{85}Rb atoms (triangles) and ^{87}Rb atoms (circles) in the mixture as a function of $z_0 - z_{\text{surf}}$, the distance between the trap center and the mirror surface during the 2 s compression phase. (b) Corresponding atom number normalized to the initial atom number before compression (for $z_0 - z_{\text{surf}} = 1.08$ mm). Error bars correspond to the standard error of the mean.

IV. CONCLUSION

We have presented a millimeter-scaled atom trap designed for an atom source dedicated to a dual species atom interferometer with quantum degenerate ensembles. The magnetic trap is based on a millimeter-sized wire structure which provides a surface trap with a large trapping volume. Our setup traps a high atom number of ^{85}Rb ($\sim 2 \times 10^9$) and ^{87}Rb ($\sim 4 \times 10^{10}$) in a mirror-MOT in less than 2 s. The cold atoms are transferred into the magnetic millimeter-trap. The loading efficiency was optimized and carefully modeled. Finally, we capture $\sim 5 \times 10^8$ atoms of ^{85}Rb and $\sim 6 \times 10^9$ atoms of ^{87}Rb at a temperature of about 200 μK. The intermediate size of the structures used to trap atoms allows us to conserve state-of-the-art MOT performances despite the proximity with the surface while keeping an efficient transfer to the magnetic trap. Moreover, the practical realization of the device can be achieved with usual laboratory techniques; in particular, it does not require micro-machining or cleanroom facilities.

The trap is compressed by bringing it closer to the Z-wire. It can potentially increase the confinement to a level compatible with the Bose-Einstein condensation. However, the short lifetime prevents our apparatus to reach the degeneracy. It is limited by collisions with background gases due to a small residual leakage that is being fixed. The experimental setup also makes it possible to focus an optical beam through the surface to create an ODT. This solution opens the way for the realization of hybrid (magnetic and optical) traps on chips, which is of great interest for the production of BEC mixtures on chip. In addition, we plan to set up an optical lattice through the chip to transport the atoms away from the surface, in order to perform atom interferometer experiments. This solution can potentially improve the control of the initial position and velocity of the atom source which is very critical for precision measurements with atom interferometry.

ACKNOWLEDGMENTS

We would like to thank A. Landragin, P. Bouyer, B. Battelier, D. Guéry-Odelin, J. Vigué, and T. Lévèque for useful discussion. This work has been partially supported through Grant No. NEXT ANR-10-LABX-0037 in the framework of the "Programme des Investissements d'Avenir," the French space national agency CNES (Centre National d'Etudes Spatiales), the Université Fédérale de Toulouse Midi-Pyrenées through the program emergence-CORSAIR, and the program Equipement-Ultitech-IRSAMC. J.A. and M.B. acknowledge support from CNES and the Région Occitanie.

[1] R. Bouchendira, P. Cladé, S. Guellati-Khélifa, F. Nez, and F. Biraben, Phys. Rev. Lett. **106**, 080801 (2011).
[2] G. Rosi, F. Sorrentino, L. Cacciapuoti, M. Prevedelli, and G. M. Tino, Nature **510**, 518 (2014).
[3] Z.-K. Hu, B.-L. Sun, X.-C. Duan, M.-K. Zhou, L.-L. Chen, S. Zhan, Q.-Z. Zhang, and J. Luo, Phys. Rev. A **88**, 043610 (2013).
[4] C. Freier, M. Hauth, V. Schkolnik, B. Leykauf, M. Schilling, H. Wziontek, H.-G. Scherneck, J. Müller, and A. Peters, J. Phys.: Conf. Ser. **723**, 012050 (2016).
[5] P. Gillot, B. Cheng, A. Imanaliev, S. Merlet, and F. Pereira Dos Santos, in *Proceedings of 30th EFTF* (York, UK, 2016).
[6] P. Berg, S. Abend, G. Tackmann, C. Schubert, E. Giese, W. P. Schleich, F. A. Narducci, W. Ertmer, and E. M. Rasel, Phys. Rev. Lett. **114**, 063002 (2015).
[7] I. Dutta, D. Savoie, B. Fang, B. Venon, C. L. Garrido Alzar, R. Geiger, and A. Landragin, Phys. Rev. Lett. **116**, 183003 (2016).
[8] I. Carusotto, L. Pitaevskii, S. Stringari, G. Modugno, and M. Inguscio, Phys. Rev. Lett. **95**, 093202 (2005).
[9] S. Dimopoulos and A. A. Geraci, Phys. Rev. D **68**, 124021 (2003).
[10] P. Wolf, P. Lemonde, A. Lambrecht, S. Bize, A. Landragin, and A. Clairon, Phys. Rev. A **75**, 063608 (2007).
[11] A. Derevianko, B. Obreshkov, and V. A. Dzuba, Phys. Rev. Lett. **103**, 133201 (2009).
[12] S. Pelisson, R. Messina, M.-C. Angonin, and P. Wolf, Phys. Rev. A **86**, 013614 (2012).
[13] M. A. Hohensee, S. Chu, A. Peters, and H. Müller, Phys. Rev. Lett. **106**, 151102 (2011).
[14] S. Dimopoulos, P. W. Graham, J. M. Hogan, and M. A. Kasevich, Phys. Rev. Lett. **98**, 111102 (2007).
[15] Y. Margalit, Z. Zhou, S. Machluf, D. Rohrlich, Y. Japha, and R. Folman, Science **349**, 1205 (2015).
[16] B. Barrett, L. Antoni-Micollier, L. Chichet, B. Battelier, P.-A. Gominet, A. Bertoldi, P. Bouyer, and A. Landragin, New J. Phys. **17**, 085010 (2015).
[17] L. Zhou, S. Long, B. Tang, X. Chen, F. Gao, W. Peng, W. Duan, J. Zhong, Z. Xiong, J. Wang, Y. Zhang, and M. Zhan, Phys. Rev. Lett. **115**, 013004 (2015).
[18] D. Schlippert, J. Hartwig, H. Albers, L. L. Richardson, C. Schubert, A. Roura, W. P. Schleich, W. Ertmer, and E. M. Rasel, Phys. Rev. Lett. **112**, 203002 (2014).
[19] A. Bonnin, N. Zahzam, Y. Bidel, and A. Bresson, Phys. Rev. A **88**, 043615 (2013).
[20] P. Hamilton, M. Jaffe, P. Haslinger, Q. Simmons, H. Müller, and J. Khoury, Science **349**, 849 (2015).
[21] M. D. Gregoire, I. Hromada, W. F. Holmgren, R. Trubko, and A. D. Cronin, Phys. Rev. A **92**, 052513 (2015).
[22] A. Miffre, M. Jacquey, M. Büchner, G. Trénec, and J. Vigué, Eur. Phys. J. D **38**, 353 (2006).
[23] W. F. Holmgren, R. Trubko, I. Hromada, and A. D. Cronin, Phys. Rev. Lett. **109**, 243004 (2012).
[24] R. H. Leonard, A. J. Fallon, C. A. Sackett, and M. S. Safronova, Phys. Rev. A **92**, 052501 (2015).
[25] C. Champenois, M. Büchner, R. Delhuille, R. Mathevet, C. Robilliard, C. Rizzo, and J. Vigué, *The Hydrogen Atom: Precision Physics of Simple Atomic Systems*, Lecture Notes in Physics Vol. 570 (Springer, 2001), p. 554.
[26] A. Arvanitaki, S. Dimopoulos, A. A. Geraci, J. Hogan, and M. Kasevich, Phys. Rev. Lett. **100**, 120407 (2008).
[27] T. Kovachy, P. Asenbaum, C. Overstreet, C. A. Donnelly, S. M. Dickerson, A. Sugarbaker, J. M. Hogan, and M. A. Kasevich, Nature **528**, 530 (2015).
[28] M. Arndt and K. Hornberger, Nat. Phys. **10**, 271 (2014).
[29] S. Nimmrichter and K. Hornberger, Phys. Rev. Lett. **110**, 160403 (2013).
[30] S. Lepoutre, A. Gauguet, G. Trénec, M. Büchner, and J. Vigué, Phys. Rev. Lett. **109**, 120404 (2012).
[31] K. S. Hardman, C. C. N. Kuhn, G. D. McDonald, J. E. Debs, S. Bennetts, J. D. Close, and N. P. Robins, Phys. Rev. A **89**, 023626 (2014).
[32] *Atom Chips*, edited by J. Reichel and V. Vuletic (Wiley-VCH, Hoboken, NJ, 2011).
[33] M. Keil, O. Amit, S. Zhou, D. Groswasser, Y. Japha, and R. Folman, J. Mod. Opt. **63**, 1840 (2016).
[34] D. M. Farkas, K. M. Hudek, E. A. Salim, S. R. Segal, M. B. Squires, and D. Z. Anderson, Appl. Phys. Lett. **96**, 093102 (2010).
[35] J. Rudolph, W. Herr, C. Grzeschik, T. Sternke, A. Grote, M. Popp, D. Becker, H. Müntinga, H. Ahlers, A. Peters, C. Lämmerzahl, K. Sengstock, N. Gaaloul, W. Ertmer, and E. M. Rasel, New J. Phys. **17**, 065001 (2015).
[36] S. Aubin, S. Myrskog, M. H. T. Extavour, L. J. LeBlanc, D. McKay, A. Stummer, and J. H. Thywissen, Nat. Phys. **2**, 384 (2006).
[37] M. K. Ivory, A. R. Ziltz, C. T. Fancher, A. J. Pyle, A. Sensharma, B. Chase, J. P. Field, A. Garcia, D. Jervis, and S. Aubin, Rev. Sci. Instrum. **85**, 043102 (2014).
[38] P. A. Altin, N. P. Robins, D. Doring, J. E. Debs, R. Poldy, C. Figl, and J. D. Close, Rev. Sci. Instrum. **81**, 063103 (2010).
[39] S. Cornish, N. Claussen, J. Roberts, E. Cornell, and C. Wieman, Phys. Rev. Lett. **85**, 1795 (2000).
[40] C. J. E. Straatsma, M. K. Ivory, J. Duggan, J. Ramirez-Serrano, D. Z. Anderson, and E. A. Salim, Opt. Lett. **40**, 3368 (2015).

[41]S. Schneider, A. Kasper, Ch. Hagen, M. Bartenstein, B. Engeser, T. Schumm, I. Bar-Joseph, R. Folman, L. Feenstra, and J. Schmiedmayer, Phys. Rev. A **67**, 023612 (2003).
[42]A. Hopkins, B. Lev, and H. Mabuchi, Phys. Rev. A **70**, 053616 (2004).
[43]K. L. Moore, T. P. Purdy, K. W. Murch, K. R. Brown, K. Dani, S. Gupta, and D. M. Stamper-Kurn, Appl. Phys. B **82**, 533 (2006).
[44]R. Wang, M. Liu, F. Minardi, and M. Kasevich, Phys. Rev. A **75**, 013610 (2007).
[45]D. Trypogeorgos, S. D. Albright, D. Beesley, and C. J. Foot, J. Phys. B: At., Mol. Opt. Phys. **47**, 075302 (2014).
[46]M. T. DePue, S. Lukman Winoto, D. J. Han, and D. S. Weiss, Opt. Commun. **180**, 73 (2000).
[47]M. P. A. Jones, C. J. Vale, D. Sahagun, B. V. Hall, and E. A. Hinds, Phys. Rev. Lett. **91**, 080401 (2003).
[48]D. Harber, J. McGuirk, J. Obrecht, and E. Cornell, J. Low Temp. Phys. **133**, 229 (2003).
[49]B. Kasch, H. Hattermann, D. Cano, T. E. Judd, S. Scheel, C. Zimmermann, R. Kleiner, D. Koelle, and J. Fortágh, New J. Phys. **12**, 065024 (2010).
[50]J. Märkle, A. J. Allen, P. Federsel, B. Jetter, A. Günther, J. Fortágh, N. P. Proukakis, and T. E. Judd, Phys. Rev. A **90**, 023614 (2014).